Potassium Metal Batteries | **Hot Paper**

Zitierweise:
Internationale Ausgabe: doi.org/10.1002/anie.202300943
Deutsche Ausgabe: doi.org/10.1002/ange.202300943

Influence of Potassium Metal-Support Interactions on Dendrite Growth

Pengcheng Liu, Dean Yen, Bairav S. Vishnugopi, Varun R. Kankanallu, Doğa Gürsoy, Mingyuan Ge, John Watt, Partha P. Mukherjee, Yu-chen Karen Chen-Wiegart, and David Mitlin**

Abstract: Combined synchrotron X-ray nanotomography imaging, cryogenic electron microscopy (cryo-EM) and modeling elucidate how potassium (K) metal-support energetics influence electrodeposit microstructure. Three model supports are employed: O-functionalized carbon cloth (potassiophilic, fully-wetted), non-functionalized cloth and Cu foil (potassiophobic, non-wetted). Nanotomography and focused ion beam (cryo-FIB) cross-sections yield complementary three-dimensional (3D) maps of cycled electrodeposits. Electrodeposit on potassiophobic support is a triphasic sponge, with fibrous dendrites covered by solid electrolyte interphase (SEI) and interspersed with nanopores (sub-10 nm to 100 nm scale). Lage cracks and voids are also a key feature. On potassiophilic support, the deposit is dense and pore-free, with uniform surface and SEI morphology. Mesoscale modeling captures the critical role of substrate-metal interaction on K metal film nucleation and growth, as well as the associated stress state.

Introduction

As the world becomes ever more electrified,[1] potassium–based electrochemical energy storage systems are emerging as another viable class of "Beyond-Li Ion" technologies for various stationary electrical energy storage systems (ESSs),[2] with potentially lower cost[3] and much greater precursor mineral abundance.[4] Potassium metal batteries (KMBs, PMBs) and potassium ion batteries (KIBs, PIBs) also possess some electrochemical advantages over lithium and sodium systems, since the ions have smaller Stokes' radius, weaker Lewis acidity and higher mobility in liquid electrolytes.[5] Yet due to its high reactivity (looser bound valence electron) potassium metal anodes are prone to display an unstable solid electrolyte interphase (SEI) as well as the related formation and growth of dendrites during electrodeposition/dissolution.[1d,6] Strategies established for stabilizing the metal anode in KMBs have been based on artificial SEI layers,[2a,7] tuned metal surface roughness,[8] optimized electrolytes,[6b,9] functional separators,[5b,10] and advanced current collector architectures.[6a,11]

It is recognized that dendrite growth will affect the integrity of the SEI.[1c,12] Moreover according to the established theory, early-stage metal dendrite nucleation and growth behavior will influence electrochemical instability during later stages of cycling.[13] However the interrelation between the energetics of the current collector-metal deposit interface and the morphology/stability of the metal-electrolyte interface is not well understood. Researchers have employed top-down scanning electron microscopy (SEM) analysis (an inherently 2D technique) to image the K metal electrodeposit.[6b,7b] This study is the first to combine synchrotron X-ray imaging and cryogenic-focused ion beam (cryo-FIB) cross-sectional SEM imaging to provide three-dimensional (3D) maps of the electrodeposition behavior of potassium metal on a wettable surface (functionalized carbon cloth) versus nonwettable surfaces (standard Cu foil, non-functionalized cloth). The obtained 3D electrodeposit morphologies and associated microstructures are highly dissimilar and have not been reported previously. The findings are explained by using mesoscale modeling, where the electrodeposit morphology is mechanistically tailored by the substrate-metal interaction.

---

[*] P. Liu, D. Mitlin
Materials Science and Engineering Program & Texas Materials Institute (TMI), The University of Texas at Austin
Austin, TX 78712-1591 (USA)
E-mail: pch060710111@hotmail.com
david.mitlin2@utexas.edu

D. Yen, V. R. Kankanallu, Y.-c. K. Chen-Wiegart
Department of Materials Science and Chemical Engineering, Stony Brook University
Stony Brook, NY 11794 (USA)

B. S. Vishnugopi, P. P. Mukherjee
School of Mechanical Engineering, Purdue University
West Lafayette, IN 47907 (USA)

D. Gürsoy
Advanced Photon Source, Argonne National Laboratory
Lemont, IL 60439 (USA)

M. Ge, Y.-c. K. Chen-Wiegart
National Synchrotron Light Source II (NSLS-II),
Brookhaven National Laboratory
Upton, NY 11973-5000 (USA)

J. Watt
Center for Integrated Nanotechnologies,
Los Alamos National Laboratory
Los Alamos, NM 87545 (USA)

Results and Discussion

A functionalized carbon cloth "FCC" with O-rich surface groups and defects was fabricated and employed as a current collector. Surface functionalization consisted of annealing cloth mixed with KOH at 700 °C in inert atmosphere, details being provided in the Experimental. Figure S1(a) provides a schematic of FCC fabrication process and illustrates the role of FCC in uniform K metal electrodeposition/electrodissolution. Figures S1(b–d) present SEM images of the as-fabricated FCC surface, taken at increasing magnification. Figure S2 presents SEM images of the baseline untreated carbon cloth "CC", indicating the two surfaces are macroscopically similar. The surface chemistry changes of FCC and CC were analyzed by X-ray photoelectron spectroscopy (XPS), Fourier-transform infrared spectroscopy (FTIR) and Raman spectroscopy. Per XPS results in Figures S1(e) and S3, it may be observed that the oxygen content of FCC is much higher than that of CC, being at 13.5 at. % vs. 1.6 at. %. This indicates the presence of oxygen-contained surface functional groups. In Figure S1(f), the peak in FTIR spectra around 1223 cm^{-1} demonstrates that these functional groups contain –O.[14] It is known that oxygen moieties promote thermal and electrochemical wettability of alkaline metals on carbon surfaces.[14b–e,15] Raman analysis in Figure S1(g) illustrates an increase in the integrated intensity ratio of D to G bands, going from 1.0 in CC to 1.34 in FCC. This is associated with the increased structural and chemical defects in carbon.[16] Surface terminating carbon defects will make that surface more energetic and likewise promote wetting by secondary phases.[17]

Figures S4–S6 show photographs that demonstrate the major enhancement in the molten K wetting behavior due to surface functionalization, comparing FCC to baseline CC and Cu. The poor wetting of baseline CC and conventional Cu foil are in Figures S4(b) and S6, showing no wetting is achieved even at 60 sec or longer time of immersion in molten metal bath. By contrast, after 1 sec the molten K has been completely infused into FCC in Figure S4(a). This structure, which will be employed for electrochemical experiments, is termed "K@FCC". In Figure S5, molten K is also infused into a larger-area sheet of FCC (5 cm^2), the process taking ≈2 sec. A video highlighting the melt infusion process for FCC, CC, Cu can be found in Movies S1–S4. The above observations confirm that FCC is potassiophilic while CC and Cu are potassiophobic, making these model systems well-suited for comparison.

Figure 1 presents a comparison of the galvanostatic cycling results for FCC and baseline Cu foil. The electrolyte employed is a carbonate system widely utilized in literature: 0.8 M KPF_6 in EC-DEC (v/v = 1:1) without any additives. A formulation of KPF_6 in EC-DEC will possess the twin advantage of low cost and oxidation stability at high voltage, making it a promising electrolyte for KIBs and KMBs to reach commercial maturity. For example, it has been shown that 0.8 M KPF_6 in EC-DEC is stable with ceramic cathodes that operate between 2–4.5 V.[5b] Ether-based electrolytes such as KFSI in DME are known to be stable at low voltages yielding improved metal anode electrochemical stability over carbonates.[6b] However it has been demonstrated that the oxidation stability of ether solvents is insufficient to enable full battery operation with ceramic cathodes.[5b] Ethers should be useful for K–S batteries where the upper voltage limit is slightly above 2 V.[18] It was not possible to achieve stable cycling with the baseline CC as the molten K would not infuse into the untreated cloth. Figure S7 shows the electrochemical performance of half-cell CC baseline. It may be observed that it is not possible to electrodeposit K metal onto the untreated cloth. The voltage never goes to zero, indicating that metal electrodeposition does not occur. Figure 1(a) shows the galvanostatic data for half-cells while Figure 1(b) shows the associated Coulombic efficiency (CE). The CE of half-cell FCC reaches up to 85 % after 120 stable cycles (11600 mins), which is the range expected when employing the KPF_6-ester-electrolyte system.[6b,9c] By contrast, for half-cell Cu after 13th cycle (860 mins) there is minimal capacity electrodissolved, with the CE close to zero.

Figures 1(c–f) display the galvanostatic data of symmetric cells, namely K@FCC||K@FCC and baseline K-Cu||K-Cu (K foil backed by standard Cu foil). With symmetric K@FCC stable electrodeposition/dissolution is achieved, for example 150 cycles (18000 mins) at a current of 0.5 $mA\,cm^{-2}$ and capacity of 0.5 $mAh\,cm^{-2}$. Even at 2 $mA\,cm^{-2}$ and 1.0 $mAh\,cm^{-2}$, the symmetric cell is stable for 100 cycles (6000 mins). In contrast, symmetric K-Cu cells at 0.5 $mA\,cm^{-2}$ are short-circuited at 26th cycle (3120 mins). The short-circuit was manifested by a sudden voltage drop to zero. Violent voltage fluctuations at each cycle are present for symmetric K-Cu at 2.0 $mA\,cm^{-2}$. An electrical "soft-short" (mixed ion-electron conduction) occurs at 19th cycle (1140 mins), leading to a sudden voltage drop albeit not entirely to zero. A more significant voltage drop occurs at 34th cycle (2040 mins), followed by a square shaped overpotential profile. This is what is expected from a full electrical short circuit with Ohmic resistance being responsible for the constant overpotential.

Figures 1(g–h) display the rate performance for symmetric K@FCC and K-Cu cells. Symmetric K@FCC can sustain a current of up to 3 $mA\,cm^{-2}$ without voltage instabilities or shorting. When the current is then turned back to 0.5 $mA\,cm^{-2}$, cells keep cycling in a stable manner. By contrast, symmetric K-Cu show large voltage fluctuations and overpotentials. Per Figure 1(h), a short circuit of K-Cu occurs at 0.1 $mA\,cm^{-2}$ after only 4 cycles (2400 mins). Table S1 shows a comparison of electrochemical performance of FCC and K@FCC versus a wide survey of the state-of-the-art literatures for K metal anodes. It may be observed that the overall electrochemical performance of half-cell FCC and symmetric K@FCC are quite favorable, especially for a generic KPF_6-carbonate solvent electrolyte system such as employed here.

Figure 2 presents a comparison of the electrodeposition/dissolution overpotentials with FCC versus baseline Cu foil at 0.5 $mA\,cm^{-2}$. First cycle galvanostatic profiles for half-cell FCC and Cu are in Figure 2(a). The Figure also illustrates how the nucleation overpotential is measured at each cycle number. The K nucleation overpotential with FCC is 12 mV, versus 300 mV with baseline Cu. These results confirm the

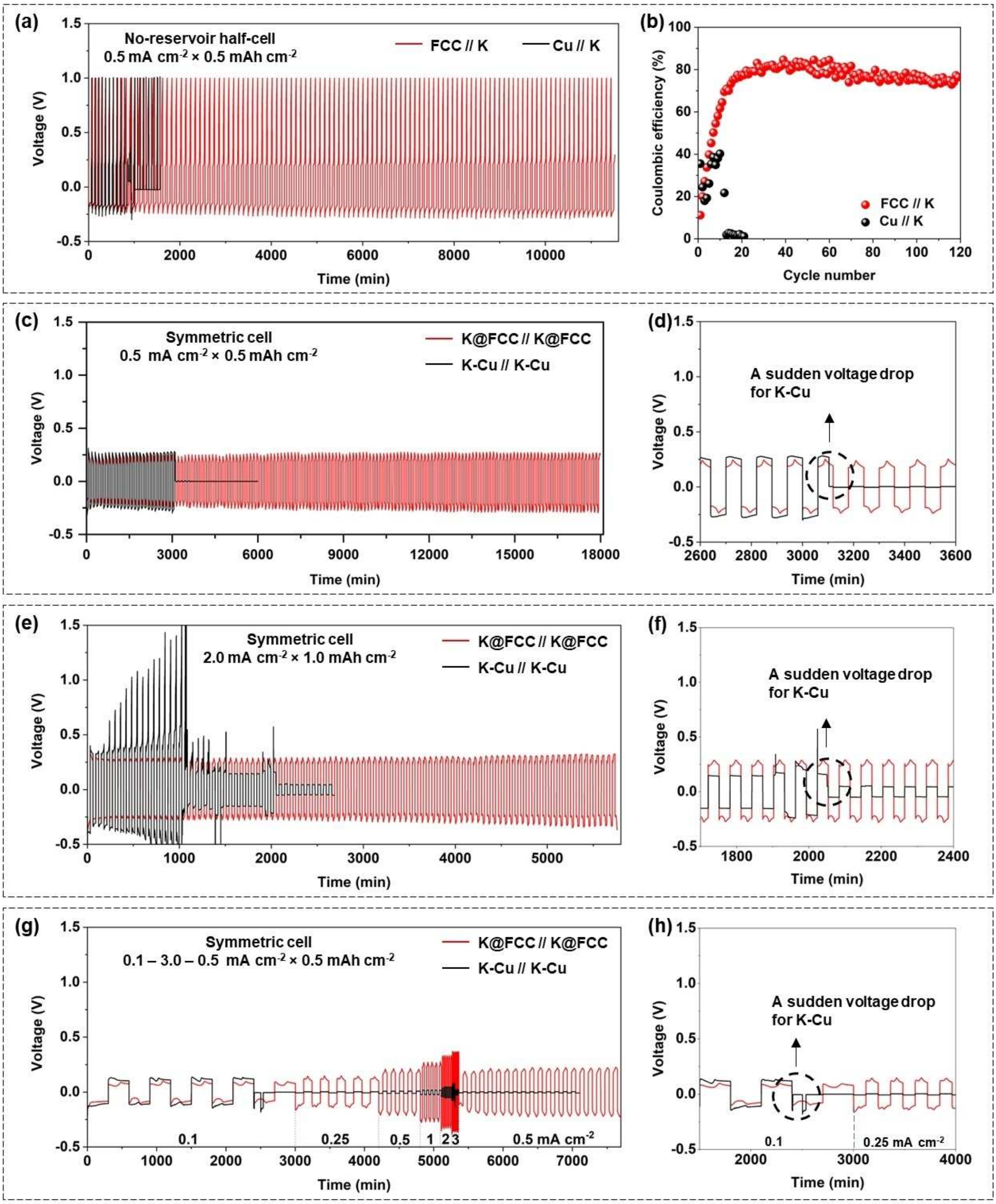

Figure 1. Electrochemical performance comparison, the current density and capacity achieved per cycle labeled directly on panels. (**a**) Galvanostatic electrodeposition-electrodissolution profiles for half-cells, FCC and baseline Cu, and (**b**) the corresponding Coulombic efficiency (CE). (**c**–**f**) Galvanostatic profiles for symmetric cells, K@FCC versus baseline K-Cu. (**g**–**h**) Galvanostatic rate results for K@FCC versus baseline K-Cu. Panels (d), (f) and (h) are enlarged profiles of portions of (c), (e) and (g).

direct link between the potassiophilicity and nucleation barrier when electrodepositing directly on an empty current collector. Figures 2(b–c) provide the evolution of electrodeposition/dissolution overpotentials for half-cell FCC and Cu, while Figures 2(e–f) show the results for symmetric cells. Throughout cycling, cells based on FCC likewise display lower and more stable overpotentials. By contrast, baseline Cu show a rapid increase in overpotentials prior to the

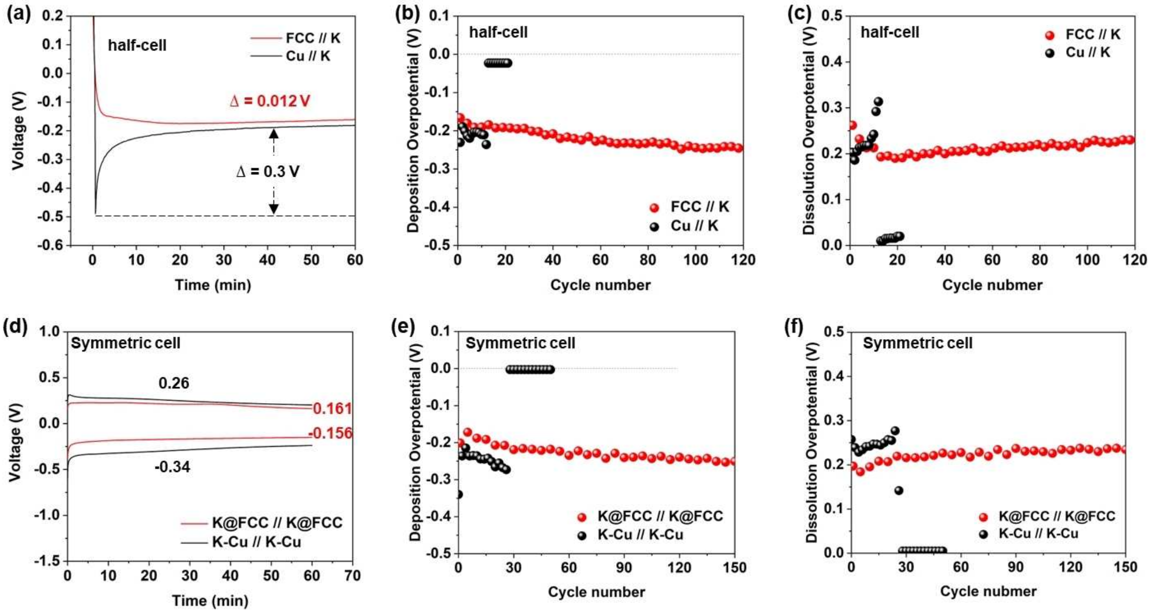

Figure 2. (**a**–**c**) Electrochemical analysis for half-cells, FCC versus baseline Cu, extracted from the 0.5 mA cm^{-2} galvanostatic profiles: Nucleation voltage profiles, electrodeposition and electrodissolution overpotentials. (**d**–**f**) Same analysis but for symmetric-cells.

electrical shorting. The overpotentials rapidly drop only once the sample is electrically shorted, with mixed electrical/ion conduction still yielding a non-zero values.[19]

Figure 2(d) shows the first cycle galvanostatic profiles for symmetric K@FCC and K-Cu. Deposition/dissolution overpotentials of symmetric cells should in principle be identical. The opposing electrodes have the same architecture, and while one is being electrodissolved the other is being electrodeposited. The cycle 1 electrodeposition overpotential of K@FCC is −0.16 V, versus −0.34 V of K-Cu. This is an interesting effect needing further understanding since in both cases electrodeposition occurs on pre-existing K metal. Likely there is preferred nucleation crystallography or even epitaxy growth associated with electrodepositing K crystallites on pre-existing K metal surfaces. We hypothesize that the microstructure of thermally infused K metal in K@FCC is more favorable for low energy nucleation than that of standard K foil used in K-Cu. The reason for this is not yet clear but may be related to the differences in grain sizes and grain crystallographic textures between two K metal films. In addition, the difference in the SEI morphology between two architectures (to be discussed) should profoundly influence the electrodeposition/dissolution overpotentials. Interrelated factors such as the variations in the SEI thickness and the stress states on support would have this effect. A reduced electrodeposition overpotential has been linked to promote planar growth rather than island-like growth of metal.[20]

Electrochemical Impedance Spectroscopy (EIS) analysis for symmetric K@FCC and K-Cu after different cycles are in Figure S8. Table S2 shows the summed charge transfer resistance and SEI resistance ($R_{CT}+R_{SEI}$) for K@FCC and K-Cu. Initially the ($R_{CT}+R_{SEI}$) values for two specimens are on-par, e.g., 728 Ω versus 745 Ω at cycle 25. At cycle 30 K-Cu electrically shorts with its Nyquist plot becoming irregular in shape and without any semicircles. But the plots of K@FCC remain stable, with a relatively minor resistance increase to 951 Ω at cycle 100. As proof-of-principle, full-cell KMBs based on Potassium hexacyanoferrate(III) $KFe^{II}Fe^{III}(CN)_6$ (one variant of Prussian blue, PB) cathode, and K@FCC or baseline K-Cu anode were fabricated. In Figures S9, a KMB based on K@FCC delivers an initial capacity of 96.1 mAh g^{-1} at 50 mA g^{-1}, with a capacity retention of 80 % after 120 cycles. Per Figure S10, K@FCC retains a capacity of 90.5 mAh g^{-1} at 100 mA g^{-1}, with a capacity retention of 84 % after 150 cycles. Figure S11 shows that K@FCC also displays more favorable rate performance. In contrast, the capacity of a KMB based on K-Cu rapidly decreases to 2.2 mAh g^{-1} after 100 cycles at 50 mA g^{-1}, corresponding to a retention of 2.3 %. The capacity rapidly decreases to 30.9 mAh g^{-1} after 150 cycles at 100 mA g^{-1}, with a retention of 33 %. Also, KMBs with K-Cu displays consistently lower CE than those with K@FCC.

Figures 3, S12 and S13 display cryo-FIB SEM analysis of the surface and cross-sections of FCC and Cu half-cells. Analysis was performed after the 5th electrodeposition at 0.5 mAh cm^{-2} and 0.5 mA cm^{-2}. In Figures 3(a–c), it may be observed that with FCC the metal electrodeposit is significantly more planar than with baseline Cu. The metal surface is largely free from metal fibers and filaments. From the cryo-FIB cross-section images in Figure 3(d), it may be observed that the bulk microstructure of the electrodeposit with FCC is dense and largely pore-free. By contrast, as shown in Figures 3(e–h) and S13, the electrodeposit on Cu is effectively a triphasic sponge composed of fiber-like dendrites interspersed with porosity and SEI (per the EDXS maps). Of course, a SEI layer also exists on the surface of metal deposit with FCC. However, per the K, C and F maps,

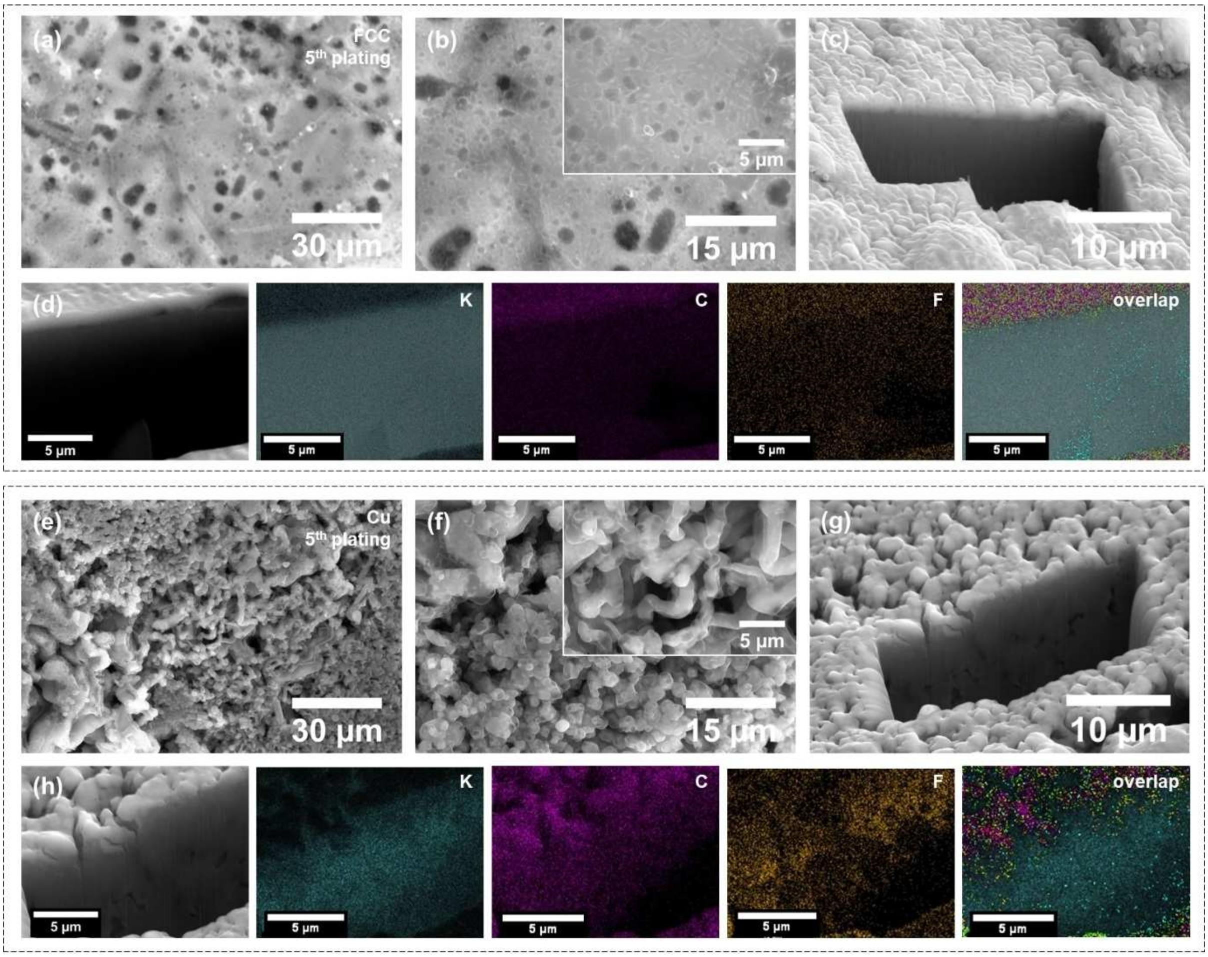

Figure 3. Cryo-FIB SEM top-down and cross-sectional analysis of FCC and baseline Cu anodes, performed after the 5th electrodeposition at 0.5 mAh cm^{-2} and 0.5 mA cm^{-2}. (**a**–**b**) Top-down images of FCC, shown at increasing magnification. (**c**–**d**) Cross-section images and EDXS K, C and F maps of FCC. (**e**–**h**) Same analysis but performed for the baseline Cu.

the SEI appears confined to the surface of films, rather than being interspersed with the metal and the pores. This is a key difference between the two morphologies, which will be further explored through synchrotron methods, surface science techniques and multiscale simulation. To confirm the generality of above findings, top-down SEM analysis was performed on half-cells that underwent cycling in an ether-based electrolyte of 4 M KFSI-DME. It should be noted that although not being suitable for high voltage cathodes, ether-based electrolytes are known to yield enhanced anode stability as compared to carbonates.[1c] Testing was performed at 0.5 mAh cm^{-2} and 0.5 mA cm^{-2}, with the 10th cycle electrodeposit being analyzed. Per Figure S14, it may be observed that the FCC electrode likewise displays a more planar electrodeposit morphology as compared to baseline Cu. The cycling CE of two half-cells is shown in Figure S15. Although the difference in CE values is not as great as with carbonate electrolytes, it is still significant.

Synchrotron X-ray nanotomography imaging was employed to obtain a three-dimensional (3D) map of the electrodeposited metal. There are some reports by using X-ray imaging for Li and Na metal batteries.[21] However such analysis has not been performed previously for the potassium metal system. Figure 4(a) shows the setup schematic of synchrotron X-ray nano-tomography at the Full Field X-ray Imaging beamline (FXI, 18-ID) at NSLS-II.[22] The detailed experimental procedure including the sample preparation, measurements, data analysis and visualization are in the Supplemental and refs.[23] Figures 4–5 show the 3D morphological analysis of electrodeposited K metal, comparing half-cell FCC versus baseline Cu. Both were analyzed after the 5th electrodeposition with 0.5 mAh cm^{-2} at 0.5 mA cm^{-2}. Figure 4(b) shows a 3D morphological overview of the electrodeposited K metal on Cu substrate. The structure is fibrous and highly porous extending beyond ≈40 µm in thickness field of view. A detailed pseudo cross-sectional view of three different orthogonal orientations (XY, YZ and XZ plane) is shown in Figure 4(c). The analysis revealed that the fine pores are on the order of tens to few hundreds of nanometers, with even smaller likely present but being beyond the resolution of the TXM. Further details of the electrodeposit are revealed in Figures 4(d–e) showing the 3D and 2D pseudo cross-sectional views from a sub-volume

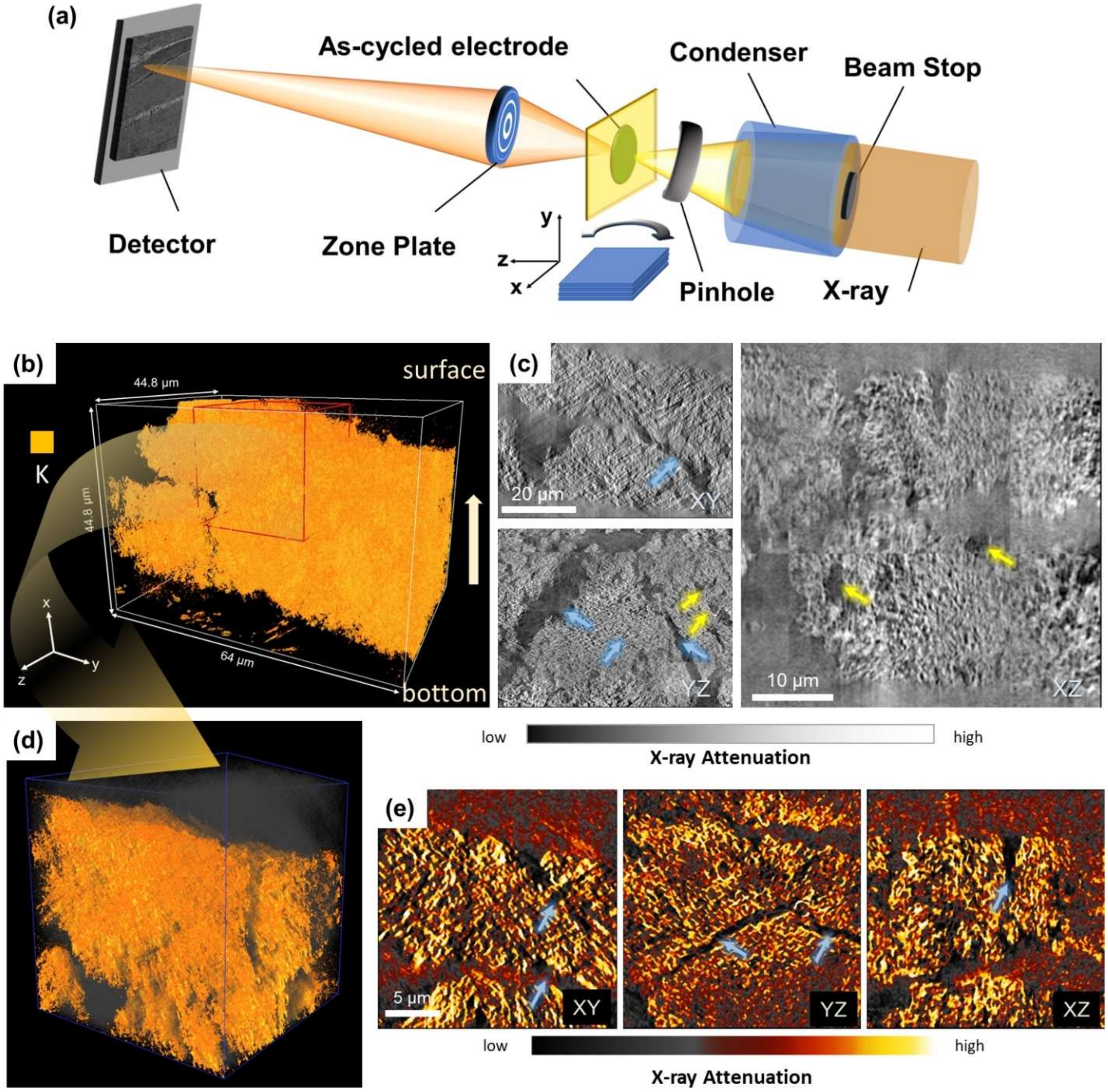

Figure 4. Synchrotron X-ray nano-tomography of electrodeposited K metal in baseline Cu half-cell. Analysis performed after the 5th electrodeposition with 0.5 $\mathrm{mAh\,cm^{-2}}$ at 0.5 $\mathrm{mA\,cm^{-2}}$. (**a**) X-ray nano-tomography setup at the FXI beamline, NSLS-II. (**b**) 3D volume rendering of K plated on Cu (Cu collector is towards the image bottom, not shown in the tomographic view but with the direction indicated), with (**c**) corresponding pseudo cross-sectional views of three different orthogonal orientations. (**d**) A zoom-in 3D view of a sub-volume from (b), and (**e**) its corresponding cross-sectional views. The blue arrows in (c) and (e) indicate the cracks and yellow arrows indicate the larger voids within highly porous dendritic structures.

of the porous structure. Movie S5 shows the 3D X-ray nano-tomography of the internal structure of the electrodeposited cell, corresponding to the sub-volume in Figure 4(d). Another feature of the electrodeposit on Cu are larger pores (yellow arrows), as well as cracks (blue arrows) that transverse the structure. This highly porous structure with cracks and large voids is correlated with poor electrochemical behavior and the associated non-wetting of the metal on the support. These morphological defects and their continuing evolution will in sum lead to the observed voltage instability and premature electrical shorting.

Figure 5 shows X-ray nano-tomography analysis for the FCC half-cells. As the carbon fibers have a relatively low X-ray attenuation, the contrast in images originates from the K metal electrodeposited around them. Figure 5(a) presents an overview of the electrodeposit which coats the O-functionalized surface in a relatively uniform manner. This may be observed from the cylindrical morphology of the metal coating around individual fibers. The volumetric and 2D pseudo cross-sectional views in Figures 5(b–c) and 5(d–e) further highlight the deposit morphology at two different scales. Movie S6 showing analysis corresponds to the sub-

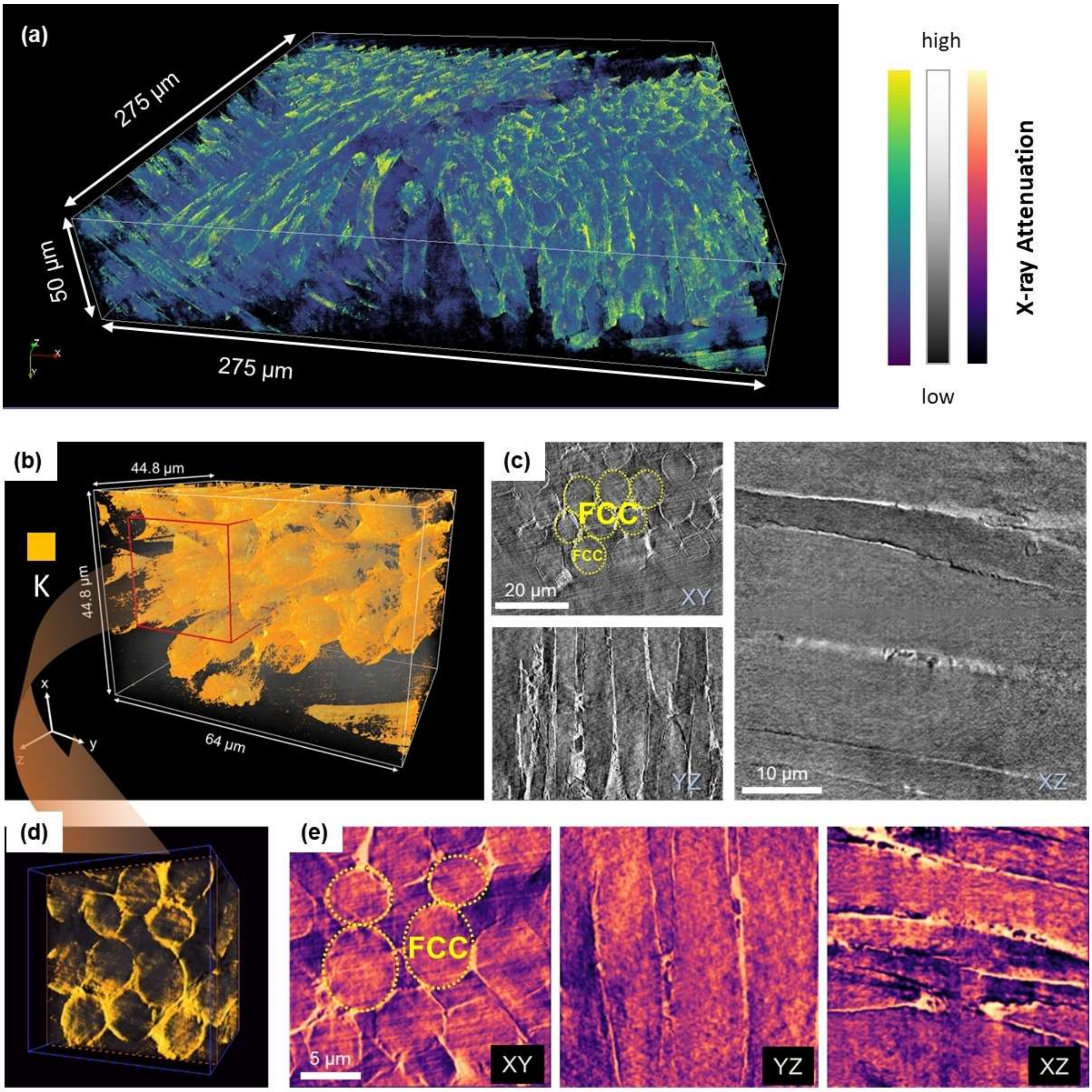

Figure 5. Synchrotron X-ray nano-tomography of electrodeposited K metal in FCC half-cell. Analysis performed after the 5th electrodeposition with 0.5 mAh cm^{-2} at 0.5 mA cm^{-2}. (**a**) An overview of the FCC electrode with relatively uniform K metal electrodeposition around the individual fibers. (**b**) 3D volume rendering of the electrodeposit on FCC substrate and (**c**) the corresponding pseudo cross-sectional views of three different orthogonal orientations. (**d**) A zoom-in 3D view of a sub-volume from (b), and (**e**) its corresponding cross-sectional views. The yellow marks in (c) and (e) indicate the representative carbon fibers of FCC.

volume in Figure 5(d). Although not fully homogeneous in its morphology, the electrodeposit on FCC is substantially more uniform than on Cu. Analogously to the electron microscopy results, there does not seem to be evidence for fibrous dendrites when FCC is employed as the support. Overall, the tomography findings are consistent with the electron microscopy results, as well as the thermal wettability and the electroanalytical findings.

Sputter etching XPS analysis was employed to further understand the differences in the SEI phase content for half-cell FCC and baseline Cu. Analysis were performed on electrodeposits after the 5th electrodeposition with 0.5 mAh cm^{-2} at 0.5 mA cm^{-2}. Figures 6(a–b) and S16 show the XPS analysis for FCC, displaying high-resolution F 1s, C 1s and survey spectra with increasing sputtering time. Figures 6(d–e) and S17 show the XPS analysis for baseline Cu at the same conditions. The integral areas of the individual peaks were obtained, allowing for an estimate of the normalized content of each component with increasing etching time. This is presented in a form of bar charts in Figures 6(c), 6(f) and S18. For both FCC and baseline Cu, the C 1s peak can be fitted into three separated peaks of

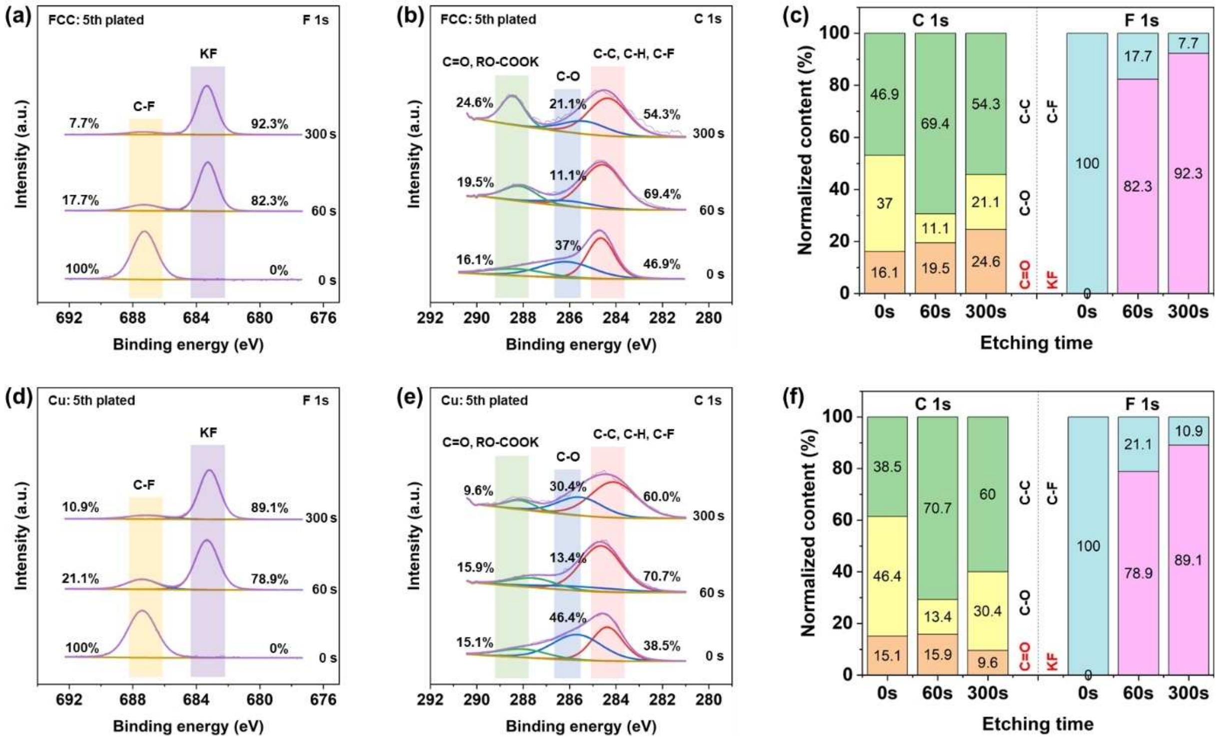

Figure 6. Sputter-down XPS spectra comparing the SEI for half-cell FCC versus Cu. Analysis performed on electrodeposits after the 5th electrodeposition with 0.5 mAh cm^{-2} at 0.5 mA cm^{-2}. (**a**–**b**) Fitted F1s and C1s spectra of FCC with increasing etching time, the relative content of phases labeled directly on panels. (**c**) Bar charts showing the relative percentage of different species in the SEI of FCC. (**d**–**f**) Same analysis but for Cu.

C–C (284.5 eV), C–O (286.0 eV), C=O & RO-COOK (288.5 eV).[24] The F 1s spectra exhibits two peaks around 682.8 (K–F) and 686.8 eV (C–F).[9a,b,25] With FCC, when the sputtering time is 0 sec (sampling ≈ top 6 nm of the SEI), only C–F is detected in F 1s spectra. When sputtering time increased to 60 sec and to 300 sec, both KF and C–F are detected, with the relative amount of KF being 82.3 % and 92.3 %, respectively. Going from 0 sec to 300 sec sputter time, the relative amount of C=O & RO-COOK increased from 16.1 % to 24.6 %. With the baseline Cu at the same sputter times, the relative content of KF increased to 78.9 % and 89.1 %, while the relative content of C=O & RO-COOK actually decreased from 15.1 % to 9.6 %. It has been reported that the presence of KF in the SEI structure should allow for enhanced mechanical toughness.[26] It has also been reported a higher polyolefin content (C=O & RO-COOK) in the SEI is beneficial for its mechanical properties.[27] The difference in the KF content between FCC and Cu is fairly minor. However the divergence in the relative polyolefin content with extended cycling may be significant enough to render the FCC SEI more robust.

To mechanistically examine the morphological evolution during the electrodeposition process, a mesoscale model was developed, with details being provided in the Supplemental and Ref. [28]. The nucleation morphology is jointly determined by the binding behavior of K on the substrate and the binding behavior of K on the freshly deposited K metal. The competing role of this interaction at the metal-substrate interface is described by using $\omega = R_{\text{K-substrate}}/R_{\text{K-K}}$ in the mesoscale model. Here, $R_{\text{K-substrate}}$ describes the adsorption kinetics of K on the substrate and $R_{\text{K-K}}$ denotes the adsorption kinetics of K on the newly formed K electrodeposits. A higher ω (i.e., $R_{\text{K-substrate}}/R_{\text{K-K}}$) mechanistically denotes an increase in the adsorption kinetics of K on the substrate when compared to the adsorption kinetics of K on the freshly deposited metal. Figure 7(a) depicts the tip height (h) of the electrodeposited morphology as a function of ω: an increase in the ω, which represents a stronger metal-substrate interaction, results in a reduced dendritic height. As shown in Figure 7(a), this regime involves an improved coverage of the metal nuclei on the substrate, eventually resulting in a homogeneous reaction front for further morphological growth. Driven by the enhancement in ω, the resultant improvement in the substrate utilization and deposition homogeneity can be inferred by comparing the morphologies in Figures 7(b–c). In contrast, a lower ω signifies a regime where preferential deposition of K takes place over the initially formed nuclei before complete coverage of the substrate, as shown in Figure 7(b). While this regime results in the formation of a non-uniform nucleation pattern, the resulting deposition structures can serve as electrochemical hotspots during the subsequent growth stage.

Figures 7(d–e), S19 and S20 depict the respective mechanical stress distributions in the SEI. The differences in the stresses are a direct outcome of the differences in the

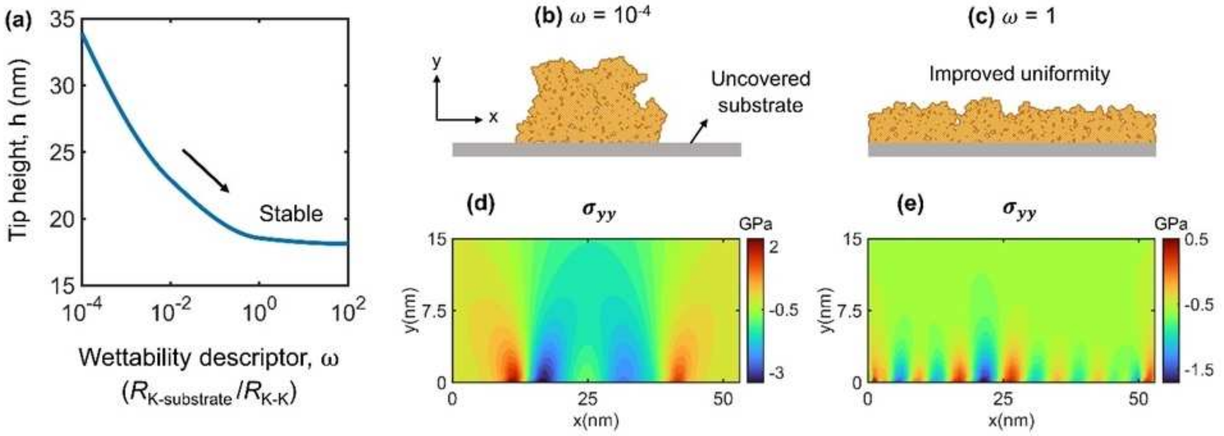

Figure 7. (**a**) Morphological tip height as a function of the wettability (ω) descriptor. (**b–c**) Role of metal-substrate interaction on the nucleation and growth morphology. The electrodeposited metal and the substrate are denoted by the orange and grey colors, respectively. (**d**, **e**) illustrate the mechanical stress along the y-direction (σ_{yy}) in the SEI for the morphologies captured in (b) and (c), respectively.

growth patterns. Figures 7(d–e) show the mechanical stresses along the y-direction (σ_{yy}), with positive and negative magnitudes corresponding to tensile and compressive stresses, respectively. Along with the decrease in substrate utilization, a reduction in the metal-substrate interaction is observed to result in localized mechanical stresses. Specifically, the morphology in Figure 7(b) imposes a large tensile stress on the SEI near the edge of the electrodeposit structure. As seen from Figure S20, these regions also experience the maximum shear stresses. Physically, a higher propensity for metal deposition over the initial nuclei (i.e., a lower ω as in Figure 7(b)) subjects the SEI to larger mechanical stresses. On the other hand, with a metal-substrate interaction improvement, the formation of a homogenized electrodeposit morphology (Figure 7(c)) leads to a more uniform stress profile (Figure 7(e)).

Conclusion

Synchrotron X-ray nanotomography imaging, cryo-FIB SEM, surface science analysis and mesoscale simulation are combined to elucidate how current collector wetting influences the three-dimensional morphology, microstructure, and SEI properties of K metal electrodeposits. Three model supports are tested in standard carbonate electrolyte (KPF_6 in EC-DEC): FCC with O-surface groups, nonfunctionalized CC and Cu foil. Wettability is correlated with dendrite-free metal film morphologies. Modeling results demonstrate the critical role of the substrate-metal interactions on planar versus dendritic growth, explaining the experimental correlation between wetting behavior, electrochemical performance and electrodeposit morphology/structure. State-of-the-art electrochemical performance is achieved in half cells, symmetric cells and full-cell PMBs with PB cathodes.

Acknowledgements

This work was supported by the U.S. Department of Energy, Office of Basic Energy Sciences, Division of Materials Sciences and Engineering under Award #DE-SC0023260. This research used resources and Full Field X-ray Imaging (FXI) beamline (18-ID) of the National Synchrotron Light Source II, a U.S. Department of Energy (DOE) Office of Science by Brookhaven National Laboratory under Contract No. DE-SC0012704. This research used resources of the Center for Functional Nanomaterials (CFN), which is a U.S. DOE Office of Science Facility, at Brookhaven National Laboratory under Contract No. DE-SC0012704. This work was performed, in part, at the Center for Integrated Nanotechnologies (CINT), an Office of Science User Facility operated for the U.S. Department of Energy (DOE) Office of Science. Los Alamos National Laboratory, an affirmative action equal opportunity employer, is managed by Triad National Security, LLC for the U.S. Department of Energy's NNSA, under contract 89233218CNA000001. Nicole Zmich is acknowledged for assisting the TXM sample preparation, and her effort is supported by an NSF NRT Award in Quantitative Analysis of Dynamic Structures (DGE 1922639) as a fellowship. Cheng-Chu Chung and Xiaoyin Zheng are acknowledged for conducting the FXI measurements. We thank Wah-Keat Lee and Xianghui Xiao, FXI beamline scientists, for their continuing efforts on the beamline development and collaboration.

Conflict of Interest

The authors declare no conflict of interest.

Data Availability Statement

The data that support the findings of this study are available from the corresponding author upon reasonable request.

Keywords: Metal Dendrite · Potassium Ion Battery · Potassium Metal Battery · Potassium Sulfur Battery

---

[1] a) L. Xue, Y. Li, H. Gao, W. Zhou, X. Lu, W. Kaveevivitchai, A. Manthiram, J. B. Goodenough, *J. Am. Chem. Soc.* **2017**, *139*, 2164; b) T. Hosaka, K. Kubota, A. S. Hameed, S. Komaba, *Chem. Rev.* **2020**, *120*, 6358; c) P. Liu, D. Mitlin, *Acc. Chem. Res.* **2020**, *53*, 1161; d) W. Zhang, Y. Liu, Z. Guo, *Sci. Adv.* **2019**, *5*, eaav7412.

[2] a) P. Liu, Y. Wang, H. Hao, S. Basu, X. Feng, Y. Xu, J. A. Boscoboinik, J. Nanda, J. Watt, D. Mitlin, *Adv. Mater.* **2020**, *32*, 2002908; b) C. Vaalma, D. Buchholz, M. Weil, S. Passerini, *Nat. Rev. Mater.* **2018**, *3*, 18013; c) M. Yu, Y. Sui, S. K. Sandstrom, C. Y. Wu, H. Yang, W. Stickle, W. Luo, X. Ji, *Angew. Chem. Int. Ed.* **2022**, *61*, e202212191; *Angew. Chem.* **2022**, *134*, e202212191; d) X. Lin, Y. Sun, Q. Sun, J. Luo, Y. Zhao, C. Zhao, X. Yang, C. Wang, H. Huo, R. Li, X. Sun, *Adv. Energy Mater.* **2021**, *11*, 2003789.

[3] a) R. Jain, P. Hundekar, T. Deng, X. Fan, Y. Singh, A. Yoshimura, V. Sarbada, T. Gupta, A. S. Lakhnot, S. O. Kim, C. Wang, N. Koratkar, *ACS Nano* **2019**, *13*, 14094; b) B. S. Vishnugopi, E. Kazyak, J. A. Lewis, J. Nanda, M. T. McDowell, N. P. Dasgupta, P. P. Mukherjee, *ACS Energy Lett.* **2021**, *6*, 3734.

[4] a) U. S. G. Survey, in *U. S. Geological Survey: Mineral Commodity Summaries*, Vol. 200 p (Ed.: A. C. Tolcin), Reston, VA, **2020**, p. https://doi.org/10.3133/mcs2020; b) J. Luo, Y. Zhang, E. Matios, P. Wang, C. Wang, Y. Xu, X. Hu, H. Wang, B. Li, W. Li, *Nano Lett.* **2022**, *22*, 1382; c) C. Wang, A. C. Thenuwara, J. Luo, P. P. Shetty, M. T. McDowell, H. Zhu, S. Posada-Perez, H. Xiong, G. Hautier, W. Li, *Nat. Commun.* **2022**, *13*, 4934; d) X. Hu, E. Matios, Y. Zhang, C. Wang, J. Luo, W. Li, *Angew. Chem. Int. Ed.* **2021**, *60*, 5978; *Angew. Chem.* **2021**, *133*, 6043; e) H. Wang, C. Wang, M. Zheng, J. Liang, M. Yang, X. Feng, X. Ren, D. Y. W. Yu, Y. Li, X. Sun, *Angew. Chem. Int. Ed.* **2023**, *62*, e202214117; *Angew. Chem.* **2023**, *135*, e202214117; f) X. Yang, X. Gao, M. Jiang, J. Luo, J. Yan, J. Fu, H. Duan, S. Zhao, Y. Tang, R. Yang, R. Li, J. Wang, H. Huang, C. Veer Singh, X. Sun, *Angew. Chem. Int. Ed.* **2023**, *62*, e202215680; *Angew. Chem.* **2023**, *135*, e202215680.

[5] a) S. Komaba, T. Hasegawa, M. Dahbi, K. Kubota, *Electrochem. Commun.* **2015**, *60*, 172; b) P. Liu, H. Hao, H. Celio, J. Cui, M. Ren, Y. Wang, H. Dong, A. R. Chowdhury, T. Hutter, F. A. Perras, J. Nanda, J. Watt, D. Mitlin, *Adv. Mater.* **2022**, *34*, 2105855; c) K. Kubota, M. Dahbi, T. Hosaka, S. Kumakura, S. Komaba, *Chem. Rec.* **2018**, *18*, 459; d) Z. Jian, W. Luo, X. Ji, *J. Am. Chem. Soc.* **2015**, *137*, 11566.

[6] a) P. Liu, Y. Wang, Q. Gu, J. Nanda, J. Watt, D. Mitlin, *Adv. Mater.* **2020**, *32*, 1906735; b) N. Xiao, W. D. McCulloch, Y. Wu, *J. Am. Chem. Soc.* **2017**, *139*, 9475; c) P. Hundekar, S. Basu, X. Fan, L. Li, A. Yoshimura, T. Gupta, V. Sarbada, A. Lakhnot, R. Jain, S. Narayanan, Y. Shi, C. Wang, N. Koratkar, *Proc. Natl. Acad. Sci. USA* **2020**, *117*, 201915470.

[7] a) H. W. Wang, J. Y. Hu, J. H. Dong, K. C. Lau, L. Qin, Y. Lei, B. H. Li, D. Y. Zhai, Y. Y. Wu, F. Y. Kang, *Adv. Energy Mater.* **2019**, *9*, 1902697; b) M. Ye, J. Y. Hwang, Y. K. Sun, *ACS Nano* **2019**, *13*, 9306.

[8] Y. Gu, W. W. Wang, Y. J. Li, Q. H. Wu, S. Tang, J. W. Yan, M. S. Zheng, D. Y. Wu, C. H. Fan, W. Q. Hu, Z. B. Chen, Y. Fang, Q. H. Zhang, Q. F. Dong, B. W. Mao, *Nat. Commun.* **2018**, *9*, 1339.

[9] a) S. Liu, J. Mao, Q. Zhang, Z. Wang, W. K. Pang, L. Zhang, A. Du, V. Sencadas, W. Zhang, Z. Guo, *Angew. Chem. Int. Ed.* **2020**, *59*, 3638; *Angew. Chem.* **2020**, *132*, 3667; b) V. Renman, D. O. Ojwang, C. Pay Gómez, T. Gustafsson, K. Edström, G. Svensson, M. Valvo, *J. Phys. Chem. C* **2019**, *123*, 22040; c) T. Hosaka, S. Muratsubaki, K. Kubota, H. Onuma, S. Komaba, *J. Phys. Chem. Lett.* **2019**, *10*, 3296; d) W. Zhang, W. K. Pang, V. Sencadas, Z. Guo, *Joule* **2018**, *2*, 1534; e) B. S. Vishnugopi, F. Hao, A. Verma, L. E. Marbella, V. Viswanathan, P. P. Mukherjee, *ACS Energy Lett.* **2021**, *6*, 2190; f) B. S. Vishnugopi, F. Hao, A. Verma, P. P. Mukherjee, *Phys. Chem. Chem. Phys.* **2020**, *22*, 11286; g) J. Chen, D. Yu, Q. Zhu, X. Liu, J. Wang, W. Chen, R. Ji, K. Qiu, L. Guo, H. Wang, *Adv. Mater.* **2022**, *34*, 2205678.

[10] a) Y. Jiang, Y. Yang, F. Ling, G. Lu, F. Huang, X. Tao, S. Wu, X. Cheng, F. Liu, D. Li, H. Yang, Y. Yao, P. Shi, Q. Chen, X. Rui, Y. Yu, *Adv. Mater.* **2022**, *34*, 2109439; b) H. Yang, F. He, M. Li, F. Huang, Z. Chen, P. Shi, F. Liu, Y. Jiang, L. He, M. Gu, Y. Yu, *Adv. Mater.* **2021**, *33*, 2106353; c) S. Wang, Y. Yan, D. Xiong, G. Li, Y. Wang, F. Chen, S. Chen, B. Tian, Y. Shi, *Angew. Chem. Int. Ed.* **2021**, *60*, 25122; *Angew. Chem.* **2021**, *133*, 25326.

[11] a) X. Tang, D. Zhou, P. Li, X. Guo, B. Sun, H. Liu, K. Yan, Y. Gogotsi, G. Wang, *Adv. Mater.* **2020**, *32*, 1906739; b) L. Qin, Y. Lei, H. Wang, J. Dong, Y. Wu, D. Zhai, F. Kang, Y. Tao, Q. H. Yang, *Adv. Energy Mater.* **2019**, *9*, 1901427; c) Y. Li, L. Zhang, S. Liu, X. Wang, D. Xie, X. Xia, C. Gu, J. Tu, *Nano Energy* **2019**, *62*, 367; d) X. Zhao, F. Chen, J. Liu, M. Cheng, H. Su, J. Liu, Y. Xu, *J. Mater. Chem. A* **2020**, *8*, 5671; e) Y. Zhao, B. Liu, Y. Yi, X. Lian, M. Wang, S. Li, X. Yang, J. Sun, *Adv. Mater.* **2022**, *34*, 2202902; f) Y. Yi, J. Li, Z. Gao, W. Liu, Y. Zhao, M. Wang, W. Zhao, Y. Han, J. Sun, J. Zhang, *Adv. Mater.* **2022**, *34*, 2202685; g) S. Li, H. Zhu, Y. Liu, Z. Han, L. Peng, S. Li, C. Yu, S. Cheng, J. Xie, *Nat. Commun.* **2022**, *13*, 4911; h) J. Meng, H. Zhu, Z. Xiao, X. Zhang, C. Niu, Y. Liu, G. Jiang, X. Wang, F. Qiao, X. Hong, F. Liu, Q. Pang, L. Mai, *ACS Nano* **2022**, *16*, 7291.

[12] a) X. B. Cheng, R. Zhang, C. Z. Zhao, Q. Zhang, *Chem. Rev.* **2017**, *117*, 10403; b) F. Hao, B. S. Vishnugopi, H. Wang, P. P. Mukherjee, *Langmuir* **2022**, *38*, 5472.

[13] a) D. R. Ely, R. E. García, *J. Electrochem. Soc.* **2013**, *160*, A662; b) B. Han, Z. Zhang, Y. Zou, K. Xu, G. Xu, H. Wang, H. Meng, Y. Deng, J. Li, M. Gu, *Adv. Mater.* **2021**, *33*, 2100404; c) X. Q. Zhang, X. Chen, R. Xu, X. B. Cheng, H. J. Peng, R. Zhang, J. Q. Huang, Q. Zhang, *Angew. Chem. Int. Ed.* **2017**, *56*, 14207; *Angew. Chem.* **2017**, *129*, 14395.

[14] a) P. G. Ren, D. X. Yan, X. Ji, T. Chen, Z. M. Li, *Nanotechnology* **2011**, *22*, 055705; b) D. Lin, Y. Liu, Z. Liang, H. W. Lee, J. Sun, H. Wang, K. Yan, J. Xie, Y. Cui, *Nat. Nanotechnol.* **2016**, *11*, 626; c) Z. Li, K. Liu, K. Fan, Y. Yang, M. Shao, M. Wei, X. Duan, *Angew. Chem. Int. Ed.* **2019**, *58*, 3962; *Angew. Chem.* **2019**, *131*, 4002; d) A. Wang, X. Hu, H. Tang, C. Zhang, S. Liu, Y. W. Yang, Q. H. Yang, J. Luo, *Angew. Chem. Int. Ed.* **2017**, *56*, 11921; *Angew. Chem.* **2017**, *129*, 12083; e) J. Luo, X. Lu, E. Matios, C. Wang, H. Wang, Y. Zhang, X. Hu, W. Li, *Nano Lett.* **2020**, *20*, 7700.

[15] a) X. Zhang, R. Lv, A. Wang, W. Guo, X. Liu, J. Luo, *Angew. Chem. Int. Ed.* **2018**, *57*, 15028; *Angew. Chem.* **2018**, *130*, 15248; b) J. Liu, Y. Li, X. Huang, G. Li, Z. Li, *Adv. Funct. Mater.* **2008**, *18*, 1448; c) S. Xia, B. Yang, H. Zhang, J. Yang, W. Liu, S. Zheng, *Adv. Funct. Mater.* **2021**, *31*, 2101168; d) X. He, Y. Ni, Y. Li, H. Sun, Y. Lu, H. Li, Z. Yan, K. Zhang, J. Chen, *Adv. Mater.* **2022**, *34*, 2106565.

[16] a) N. Sharma, V. Sharma, Y. Jain, M. Kumari, R. Gupta, S. K. Sharma, K. Sachdev, *Macromol. Symp.* **2017**, *376*, 1700006; b) X. Cao, D. Qi, S. Yin, J. Bu, F. Li, C. F. Goh, S. Zhang, X. Chen, *Adv. Mater.* **2013**, *25*, 2957.

[17] a) Q. Yang, M. Cui, J. Hu, F. Chu, Y. Zheng, J. Liu, C. Li, *ACS Nano* **2020**, *14*, 1866; b) J. Yi, J. Chen, Z. Yang, Y. Dai, W. Li, J. Cui, F. Ciucci, Z. Lu, C. Yang, *Adv. Energy Mater.* **2019**, *9*, 1901796.

[18] J. Ding, H. Zhang, W. Fan, C. Zhong, W. Hu, D. Mitlin, *Adv. Mater.* **2020**, *32*, 1908007.

[19] P. Albertus, S. Babinec, S. Litzelman, A. Newman, *Nat. Energy* **2018**, *3*, 16.

[20] a) L. Guo, G. Oskam, A. Radisic, P. M. Hoffmann, P. C. Searson, *J. Phys. D* **2011**, *44*, 443001; b) O. G. Bagmut, *Funct. Mater.* **2019**, *26*, 6–15.

[21] a) K. R. Adair, M. N. Banis, Y. Zhao, T. Bond, R. Li, X. Sun, *Adv. Mater.* **2020**, *32*, 2002550; b) J. Li, N. Sharma, Z. Jiang, Y. Yang, F. Monaco, Z. Xu, D. Hou, D. Ratner, P. Pianetta, P. Cloetens, F. Lin, K. Zhao, Y. Liu, *Science* **2022**, *376*, 517; c) G. Zan, G. Qian, S. Gul, H. Pan, Q. Li, J. Li, D. J. Vine, S. Lewis, W. Yun, P. Pianetta, H. Li, X. Yu, Y. Liu, *ACS Mater. Lett.* **2021**, *3*, 1786; d) G. Zan, S. Gul, J. Zhang, W. Zhao, S. Lewis, D. J. Vine, Y. Liu, P. Pianetta, W. Yun, *Proc. Natl. Acad. Sci. USA* **2021**, *118*, e2103126118; e) F. Sun, L. Duchêne, M. Osenberg, S. Risse, C. Yang, L. Chen, N. Chen, Y. Huang, A. Hilger, K. Dong, T. Arlt, C. Battaglia, A. Remhof, I. Manke, R. Chen, *Nano Energy* **2021**, *82*, 105762.

[22] D. S. Coburn, E. Nazaretski, W. Xu, M. Ge, C. Longo, H. Xu, K. Gofron, Z. Yin, H. H. Chen, Y. Hwu, W. K. Lee, *Rev. Sci. Instrum.* **2019**, *90*, 053701.

[23] a) C. H. Lin, K. Sun, M. Ge, L. M. Housel, A. H. McCarthy, M. N. Vila, C. Zhao, X. Xiao, W. K. Lee, K. J. Takeuchi, E. S. Takeuchi, A. C. Marschilok, Y. K. Chen-Wiegart, *Sci. Adv.* **2020**, *6*, eaay7129; b) C.-H. Lin, Z. Ju, X. Zheng, X. Zhang, N. Zmich, X. Liu, K. J. Takeuchi, A. C. Marschilok, E. S. Takeuchi, M. Ge, G. Yu, Y.-c. K Chen-Wiegart, *Carbon* **2022**, *188*, 114.

[24] a) K. N. Wood, G. Teeter, *ACS Appl. Energy Mater.* **2018**, *1*, 4493; b) S. Oswald, F. Thoss, M. Zier, M. Hoffmann, T. Jaumann, M. Herklotz, K. Nikolowski, F. Scheiba, M. Kohl, L. Giebeler, D. Mikhailova, H. Ehrenberg, *Batteries* **2018**, *4*, 36; c) S. Stankovich, D. A. Dikin, R. D. Piner, K. A. Kohlhaas, A. Kleinhammes, Y. Jia, Y. Wu, S. T. Nguyen, R. S. Ruoff, *Carbon* **2007**, *45*, 1558; d) D. Yang, A. Velamakanni, G. Bozoklu, S. Park, M. Stoller, R. D. Piner, S. Stankovich, I. Jung, D. A. Field, C. A. Ventrice, R. S. Ruoff, *Carbon* **2009**, *47*, 145; e) A. Siokou, F. Ravani, S. Karakalos, O. Frank, M. Kalbac, C. Galiotis, *Appl. Surf. Sci.* **2011**, *257*, 9785; f) L. Stobinski, B. Lesiak, A. Malolepszy, M. Mazurkiewicz, B. Mierzwa, J. Zemek, P. Jiricek, I. Bieloshapka, *J. Electron Spectrosc. Relat. Phenom.* **2014**, *195*, 145.

[25] Q. Zhang, J. Mao, W. K. Pang, T. Zheng, V. Sencadas, Y. Chen, Y. Liu, Z. Guo, *Adv. Energy Mater.* **2018**, *8*, 1703288.

[26] a) H. Wang, D. Yu, X. Wang, Z. Niu, M. Chen, L. Cheng, W. Zhou, L. Guo, *Angew. Chem. Int. Ed.* **2019**, *58*, 16451; *Angew. Chem.* **2019**, *131*, 16603; b) L. Deng, Y. Zhang, R. Wang, M. Feng, X. Niu, L. Tan, Y. Zhu, *ACS Appl. Mater. Interfaces* **2019**, *11*, 22449.

[27] a) Y. Gao, Z. Hou, R. Zhou, D. Wang, X. Guo, Y. Zhu, B. Zhang, *Adv. Energy Mater.* **2022**, *32*, 2112399; b) B. Lee, E. Paek, D. Mitlin, S. W. Lee, *Chem. Rev.* **2019**, *119*, 5416.

[28] a) B. S. Vishnugopi, F. Hao, A. Verma, P. P. Mukherjee, *ACS Appl. Mater. Interfaces* **2020**, *12*, 23931; b) B. S. Vishnugopi, M. B. Dixit, F. Hao, B. Shyam, J. B. Cook, K. B. Hatzell, P. P. Mukherjee, *Adv. Energy Mater.* **2022**, *12*, 2102825; c) A. F. Voter, in *Radiation Effects in Solids* (Eds.: K. E. Sickafus, E. A. Kotomin, B. P. Uberuaga), Springer Netherlands, Dordrecht, **2007**, pp. 1–23.

Manuscript received: January 30, 2023
Accepted manuscript online: March 9, 2023
Version of record online: ■■, ■■

Forschungsartikel

Potassium Metal Batteries

P. Liu,* D. Yen, B. S. Vishnugopi,
V. R. Kankanallu, D. Gürsoy, M. Ge, J. Watt,
P. P. Mukherjee, Y.-c. K. Chen-Wiegart,
D. Mitlin* **e202300943**

Influence of Potassium Metal-Support Interactions on Dendrite Growth

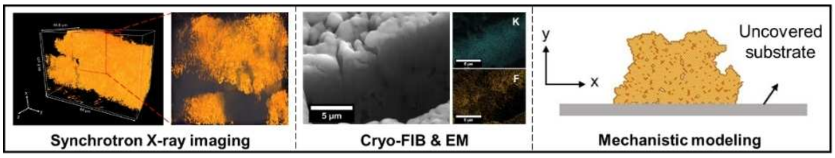

Synchrotron X-ray nanotomography imaging, cryogenic-electron microscopy (cryo-EM), and mesoscale modeling are combined to explain how the potassium metal-support energetics influence the electrodeposit microstructure. Wettability critically influences the nucleation response, the growing film morphology and associated stress state, and the propensity for dendritic growth.